

# UC Berkeley

## UC Berkeley Previously Published Works

### Title

Atomic Resolution Imaging of Halide Perovskites

### Permalink

<https://escholarship.org/uc/item/3v22r6g4>

### Journal

Nano Letters, 16(12)

### ISSN

1530-6984

### Authors

Yu, Y  
Zhang, D  
Kisielowski, C  
[et al.](#)

### Publication Date

2016-12-14

### DOI

10.1021/acs.nanolett.6b03331

Peer reviewed

# Atomic Resolution Imaging of Halide Perovskites

Yi Yu,<sup>†,‡</sup> Dandan Zhang,<sup>†,‡</sup> Christian Kisielowski,<sup>§</sup> Letian Dou,<sup>†,‡</sup> Nikolay Kornienko,<sup>†,‡</sup>  
 Yehonadav Bekenstein,<sup>†,‡</sup> Andrew B. Wong,<sup>†,‡</sup> A. Paul Alivisatos,<sup>†,‡,||,⊥</sup> and Peidong Yang<sup>\*,†,‡,||,⊥</sup>

<sup>†</sup>Department of Chemistry, University of California, Berkeley, California 94720, United States

<sup>‡</sup>Materials Sciences Division and <sup>§</sup>The Molecular Foundry Lawrence Berkeley National Laboratory, Berkeley, California 94720, United States

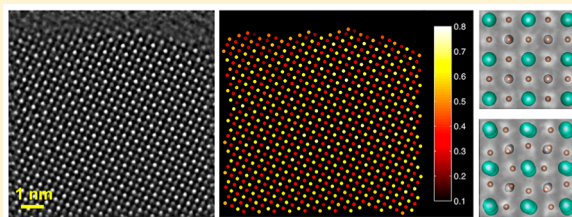
<sup>||</sup>Kavli Energy NanoScience Institute, Berkeley, California 94720, United States

<sup>⊥</sup>Department of Materials Science and Engineering, University of California, Berkeley, California 94720, United States

**S** Supporting Information

**ABSTRACT:** The radiation-sensitive nature of halide perovskites has hindered structural studies at the atomic scale. We overcome this obstacle by applying low dose-rate in-line holography, which combines aberration-corrected high-resolution transmission electron microscopy with exit-wave reconstruction. This technique successfully yields the genuine atomic structure of ultrathin two-dimensional CsPbBr<sub>3</sub> halide perovskites, and a quantitative structure determination was achieved atom column by atom column using the phase information on the reconstructed exit-wave function without causing electron beam-induced sample alterations. An extraordinarily high image quality enables an unambiguous structural analysis of coexisting high-temperature and low-temperature phases of CsPbBr<sub>3</sub> in single particles. On a broader level, our approach offers unprecedented opportunities to better understand halide perovskites at the atomic level as well as other radiation-sensitive materials.

**KEYWORDS:** Atomic resolution, halide perovskites, low dose-rate, in-line holography, radiation-sensitive materials



Halide perovskites have great potential for many applications such as high-efficiency photovoltaic cells.<sup>1</sup> Research addressing these materials, in particular their nanostructures, has recently attracted worldwide attention. Various morphologies of halide perovskites, such as quantum dots,<sup>2,3</sup> nanowires,<sup>4</sup> nanosheets (NSs),<sup>4–6</sup> and thin films,<sup>1</sup> have been fabricated and their optoelectronic properties were explored. However, structure–property relationships are difficult to extract because atomic resolution imaging of halide perovskites by transmission electron microscopy (TEM) is greatly impeded by destructive electron beam–sample interactions.<sup>4–7</sup>

Conventional TEM, aberration-corrected TEM (AC-TEM), and aberration-corrected scanning transmission electron microscopy (AC-STEM) have greatly contributed to the characterization of oxide perovskites with a spatial resolution less than one angstrom.<sup>8,9</sup> As a result of such investigations, the correlation of structure with chemical and physical properties contributes to the discovery and understanding of novel and unique properties in these materials.<sup>10–12</sup> By comparison, a precise understanding of halide perovskites is relatively underdeveloped because of their electron beam-sensitivity<sup>4–7</sup> that prohibits capturing high-resolution TEM (HRTEM) or AC-HRTEM images with commonly used electron dose rates of  $10^4$ – $10^5$  e  $\text{\AA}^{-2}$  s<sup>-1</sup>. The acquisition of HRSTEM or AC-HRSTEM images in no way relaxes this situation as these methods require even larger electron doses to form images.<sup>13,14</sup>

Making things even more challenging, electron-beam induced sample alterations occur much more quickly and severely in nanosized halide perovskites compared to the bulk material. Therefore, structural characterizations using electron beams generally have to be performed at low magnifications, where the required dose-rate to obtain sufficient contrast is much lower. Even in this situation, structural damage occurs and is evident as tiny precipitates or voids in reported TEM and STEM images.<sup>4–7</sup> Therefore, a very limited number of conventional HRTEM images supported reports<sup>2–6</sup> and the images suffered from varying degrees of blurring or distortion caused by the imaging electrons. Clearly, it is hardly possible to make further progress without addressing the problem of sample degradation during observation. So far, faithful atomic resolution images have been neither captured by electron microscopy nor any other experimental techniques for these materials.

In the present work, we visualize for the first time the pristine structure of ultrathin two-dimensional (2D) CsPbBr<sub>3</sub> halide perovskites with atomic resolution by applying low dose-rate in-line holography. This emerging method minimizes electron beam-induced sample alterations by effectively controlling electron beam-induced object excitations.<sup>15</sup> This is a low dose

**Received:** August 8, 2016

**Revised:** October 17, 2016

73 technique that retards structural damage while high signal-to-  
74 noise are generated by recording an image series that is  
75 subsequently reconstructed to extract the phase information  
76 and recover electron exit-wave functions<sup>16–18</sup> (In general,  
77 phase information is always missing in TEM images where only  
78 amplitude information preserves.) This process provides  
79 valuable phase information that enables a quantitative structure  
80 determination of 2D NSs on the basis of detecting the element-  
81 specific contrast from single atoms.

82 Atomically thin 2D CsPbBr<sub>3</sub> NSs were successfully  
83 synthesized via a catalyst-free, solution-phase method (SI  
84 section 1). The NSs were characterized using X-ray diffraction  
85 (XRD) (Figure S1a), low-magnification TEM and STEM  
86 (Figure S1b), energy-dispersive X-ray spectroscopy (EDS)  
87 (Figure S2a), and atomic force microscopy (AFM) (Figure  
88 S2b). The edge length of CsPbBr<sub>3</sub> NSs was measured to be  
89 around 100 nm, while the thickness of the NSs was a few  
90 atomic layers. An AFM image of NSs with 1–3 layer thickness  
91 is depicted in Figure S2b. The CsPbBr<sub>3</sub> bulk crystals exhibit a  
92 cubic structure at high temperature (above 403 K) and an  
93 orthorhombic crystal structure at room temperature. The cubic  
94 unit cell of CsPbBr<sub>3</sub> is illustrated in Figure 1a and a model of a  
95 2D monolayer is depicted in Figure 1b. The difference between  
96 the cubic and orthorhombic structures lies in the tilting of the  
97 Pb–Br<sub>6</sub> octahedrons in the orthorhombic case, which is difficult

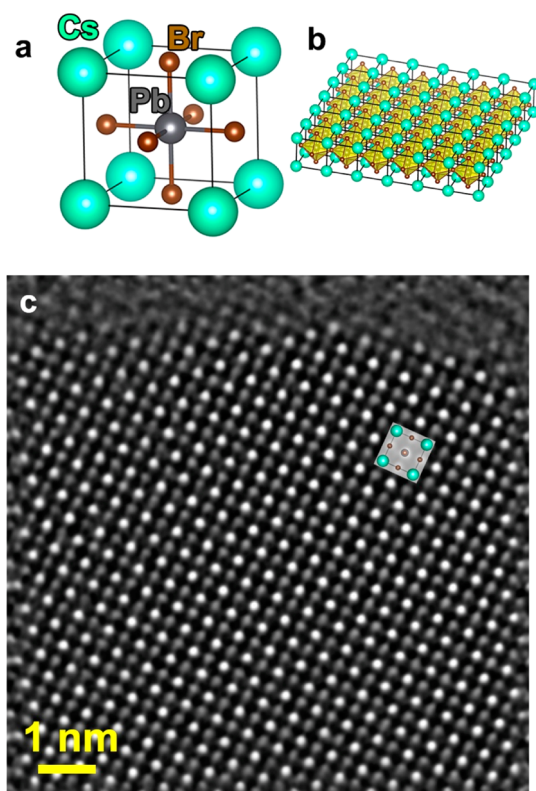


**Figure 1.** Atomic resolution image of 2D halide perovskite CsPbBr<sub>3</sub>. (a) Structure model of cubic CsPbBr<sub>3</sub> perovskite unit cell. Cs (green) occupies the corner A-site while Pb (gray) occupies the body-center B-site, and Br (brown) occupies the face-center. Pb–Br<sub>6</sub> octahedron is formed within the Cs cube framework. (b) Structure model of single layer 2D CsPbBr<sub>3</sub> NS. (c) Atomically resolved phase image of a 2D CsPbBr<sub>3</sub> NS obtained by reconstructing 80 low dose-rate AC-HRTEM images via exit-wave reconstruction. The [001] structure projection of a unit cell is overlaid on the image.

to capture with standard TEM techniques. Previous reports<sup>98</sup>  
suggest that the high-temperature phase could be stabilized in  
99 quantum dots and NSs.<sup>2,5,6</sup> However, we emphasize that  
100 Scherrer peak broadening in nanocrystals sometimes impedes  
101 the ability to distinguish the orthorhombic phase from the cubic  
102 one by peak-splitting (Figure S1a). Therefore, assignment of  
103 phases simply by conventional XRD as previously reported is  
104 insufficient and direct atomic resolution imaging is mandatory  
105 for unambiguous structure determination. 106

The ultrathin nature of CsPbBr<sub>3</sub> 2D NSs renders them prone  
107 to electron beam-induced alterations (Figures S3 and S4). We  
108 have performed comparative experiments at different accelerat-  
109 ing voltages (80 kV and 300 kV) using different imaging modes  
110 (TEM and STEM) to explore how to minimize electron beam-  
111 induced sample alterations and achieve atomic resolution. In  
112 particular, we use low dose AC-HRTEM at 80 kV (SI Sections  
113 7 and 8) to capture in-line holograms. The method addresses  
114 the shot noise problem in low dose images by acquiring an  
115 image series and solving the phase problem to reconstruct exit-  
116 wave functions.<sup>16–18</sup> For a typical reconstruction process, a  
117 focal-series of 10–100 images is recorded to recover the  
118 specimen's exit-wave function, which contains the full  
119 information from the elastic scattering process in the form of  
120 amplitude and phase images over the spatial frequencies that  
121 are relevant to form atomically resolved images. All of this data  
122 is intrinsically quantitative and can be fine-tuned even further  
123 by a posteriori aberration correction using numerical wave  
124 processing.<sup>19–21</sup> The reconstructed wave function from low  
125 dose-rate images represents a time average over the duration of  
126 the recording time that exhibits a better signal-to-noise ratio  
127 because it eliminates the well-known contrast reduction by the  
128 Stobbs factor and constitutes a weak-excitation approach that  
129 improves on sample integrity.<sup>15</sup> Therefore, the pristine  
130 structure of nanocrystals can be better maintained by this low  
131 dose-rate technique. 132

An example of a focal-series containing 80 AC-HRTEM  
133 images that were acquired at the edge of a CsPbBr<sub>3</sub> NS with a  
134 dose-rate of  $\sim 100 \text{ e}^- \text{ \AA}^{-2} \text{ s}^{-1}$  is shown in Figure S5a. The exit-  
135 wave was reconstructed from all the 80 images and the  
136 reconstructed phase image is shown in Figure 1c. It is evident  
137 that all the atom columns are clearly resolved and the contrast  
138 is homogeneous across the whole image. The homogeneous  
139 contrast is only possible if formation of vacancies, voids, or  
140 other electron beam-induced precipitates does not occur. The  
141 same conclusion can be derived by directly inspecting the  
142 contrast of all 80 sequential images (Figure S5a). The CsPbBr<sub>3</sub>  
143 NS in Figure 1c shows a perfect cubic perovskite structure in  
144 the [001] projection with the Cs atom columns and Pb–Br  
145 atom columns exhibiting higher contrast while the Br atom  
146 columns show weaker contrast. The cubic [001] atomic model  
147 is overlaid on Figure 1c and matches the experimental atom  
148 positions. The distinction between Cs columns and Pb–Br  
149 columns can be achieved by a quantitative statistical phase  
150 analysis as detailed later. The contrast maxima in Figure 1c  
151 mark the atom column positions while the intensities  
152 correspond to phase values that are determined by their  
153 chemical composition. Therefore, all necessary information can  
154 be extracted to characterize the crystal structure. The result is  
155 shown in Figure 2a. Atom positions were obtained by a  
156 least-squares fit to the intensity distribution around contrast  
157 maxima using 2D Gaussian profiles.<sup>22</sup> Phase changes were characterized  
158 by the peak-to-valley intensities of each atom column. Element  
159 specific phase changes are larger for Cs and Pb–Br columns  
160

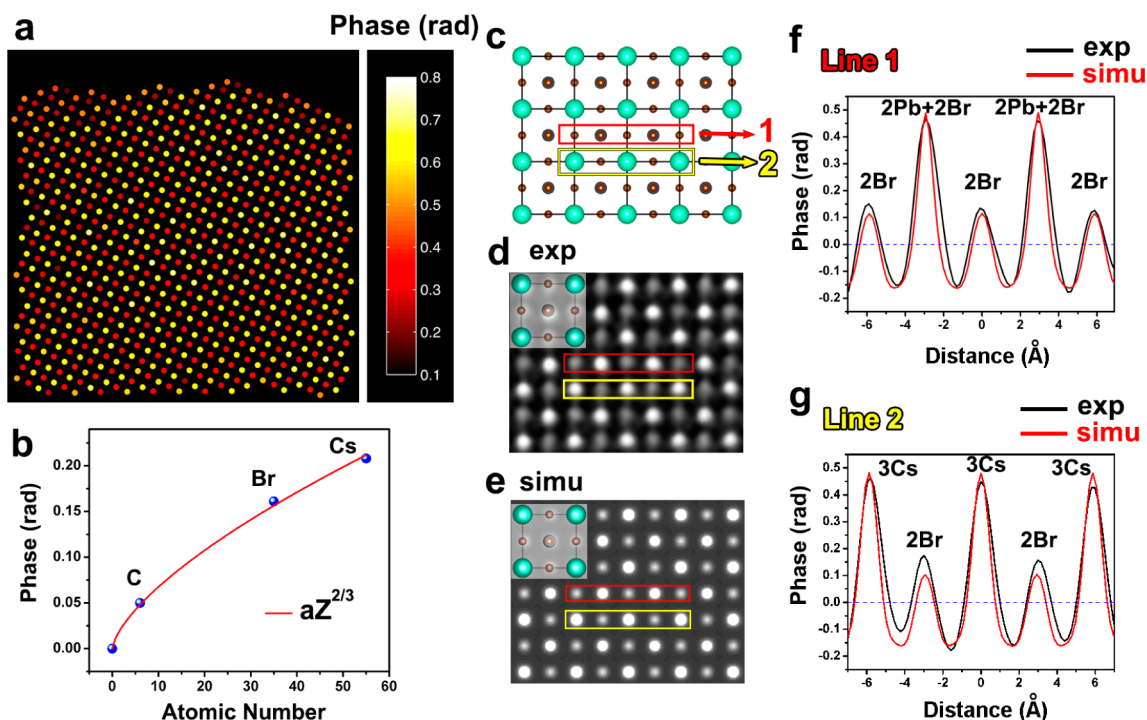


**Figure 2.** Quantitative phase analysis. (a) Atomic-scale 2D phase mapping. (b) Plot of the single atom-induced phase changes of different atom species versus their atomic number,  $Z$ . The red curve shows the fitting to the power law  $aZ^{2/3}$ , where  $a$  is a constant. Br and Cs data come from this work, while the data for C come from refs 23 and 24. (c) Model of [001] structural projection (4 unit cell by 3 unit cell). (d) Enlarged experimental phase image from a region in the center of Figure 1c. The structural model is overlaid. (e) Simulated phase image corresponds to (d). (f,g) Line profiles of two line scans (f shows line 1 and g shows line 2) as indicated in (c–e). In the profiles, black lines correspond to the experiments and red lines correspond to the simulations.

161 (yellow color) but smaller for Br columns (red color) because it  
 162 is a lighter element. The small scattering difference between Cs  
 163 columns and Pb–Br columns can only be distinguished by  
 164 comparing the average phase values of the different lattice sites  
 165 because the heavier Pb–Br columns should have slightly larger  
 166 phase change because of the electron channeling effect.<sup>20</sup> A  
 167 statistical analysis reveals that average phase values of the Cs,  
 168 Pb–Br, and Br atom columns are  $0.625 \pm 0.006$ ,  $0.640 \pm 0.006$ ,  
 169 and  $0.322 \pm 0.004$  rad, respectively, with a 95% confidence  
 170 level. These small error bars are the key to differentiate between  
 171 Cs and Pb–Br columns experimentally and are in agreement  
 172 with our simulation (Figure S7).

173 Within an extinction distance for electron channeling, the  
 174 phase increases linearly with depth.<sup>20</sup> Hence, it is not only  
 175 possible to determine the crystal structure and to identify  
 176 elements but also to determine the crystal thickness. Figure 2d  
 177 shows an enlarged phase image extracted from the center of  
 178 Figure 1c. The corresponding structural projection is depicted  
 179 in Figure 2c. For comparison, a simulated phase image of a two-  
 180 atomic-layer-thick CsPbBr<sub>3</sub> NS is shown in Figure 2e. Two line  
 181 profiles are extracted from the experimental and simulated  
 182 phase images, and the results are shown in Figure 2f,g,  
 183 respectively. The quantitative match between experimental and  
 184 simulated data indicates that the CsPbBr<sub>3</sub> NS of Figure 1c is  
 185 composed of only two atomic layers (also see Figure S8).  
 186 Knowing the crystal thickness in terms of the number of atoms  
 187 per column, we can further obtain the characteristic phase shift  
 188 per single atom. The scattering of 80 kV electrons at single Cs  
 189 and Br atoms were calculated  $0.208 \pm 0.002$  and  $0.161 \pm 0.002$   
 190 rad, respectively, and these are depicted in Figure 2b together  
 191 with an experimental value for the phase shift at a single carbon

atom reported previously.<sup>23,24</sup> All the data can be described well  
 by the power law for phase shifts caused by electron scattering  
 from a single atom that is expected to be roughly proportional  
 to  $Z^{2/3}$  ( $Z$  is the atomic number).<sup>25,26</sup> Independently of our  
 image simulation, these quantitative phase measurements can  
 be used to support the interpretation that our CsPbBr<sub>3</sub> NS are  
 indeed double-layers. Moreover, we can also compare  
 individual AC-HRTEM images of the focal-series with  
 corresponding simulated images at the measured focus values.  
 We found that experimental images fit well with the simulation  
 when the thickness is assumed to be a double-layer (Figures  
 SSb and Figure S6). Therefore, low dose-rate in-line  
 holography not only reveals the pristine structure of beam-  
 sensitive materials with atomic resolution but also allows  
 identifying elements together with the local column thickness,  
 which enables electron tomography from single projections.

Beyond a description of crystallographically perfect CsPbBr<sub>3</sub>  
 NSs, it is interesting to study structural deviations. Apart from  
 cubic structure, we have also observed orthorhombic domains  
 in some of the 2D NSs. Awareness of a possible coexistence of  
 both the high-temperature cubic phase and the room-  
 temperature orthorhombic phase is of value to the community.  
 Different from the ensemble-level information obtained from  
 X-ray techniques, our atomic-scale direct imaging method on  
 the single sheet level enables us to explore the structure more  
 deeply. The existence of the orthorhombic structure as well as  
 the coexistence of two phases can be confirmed using in-line  
 holography with different dose-rates. The results are depicted in  
 Figures S9 and S10. More details of coexistence of two phases  
 are provided in the SI Section 11. Here, apart from using the in-  
 line holography method, we demonstrate that a single AC-

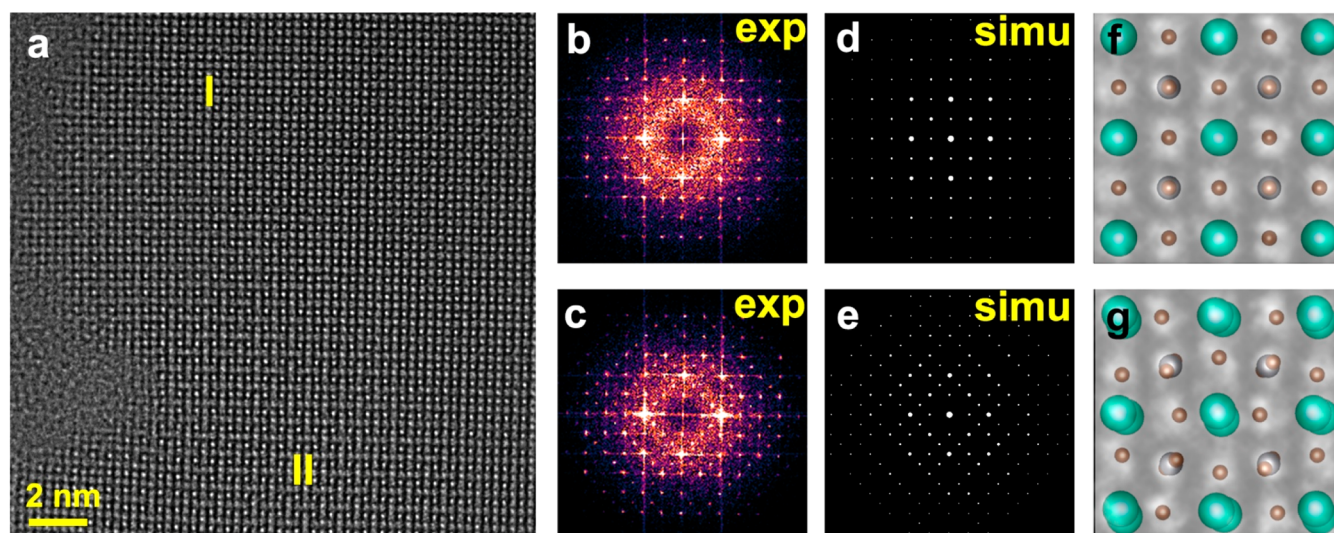


**Figure 3.** Coexistence of cubic and orthorhombic CsPbBr<sub>3</sub> within single AC-HRTEM image. (a) Experimental AC-HRTEM image with two regions denoted as I and II. (b,c) Experimental Fourier transforms from region I (b) and II (c). (d,e) Simulated electron diffraction of cubic (d) and orthorhombic (e) CsPbBr<sub>3</sub>. (f,g) Enlarged images from region I (f) and II (g). The cubic and orthorhombic structure models are overlaid on (f) and (g), respectively.

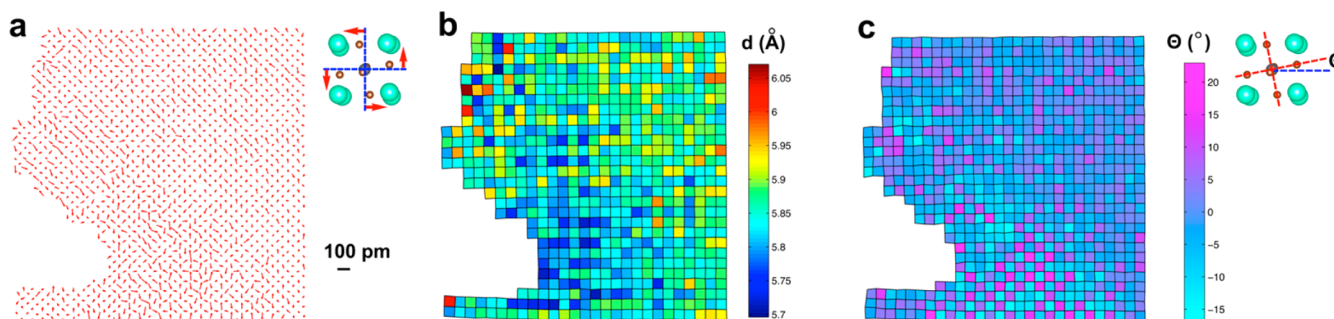


**Figure 4.** Quantitative structure analysis. (a) Br displacement map. The Br displacement is defined as the deviation of Br columns from the center of two neighboring Cs columns, as illustrated in the upper right model. The length of the red arrows represents the modulus of the displacements with respect to the scale bar in the lower right corner. The arrowheads point into the displacement directions. (b) Lattice distance map. The lattice distance is defined as the distance between two neighboring Pb–Br columns. (c) Octahedron tilting map. The tilting angle is defined as the model shown on the upper right corner.

223 HRTEM image can also be utilized to determine structural  
 224 details as long as the dose-rate is sufficiently controlled and the  
 225 material can maintain its structure at the given dose-rate. **Figure**  
 226 **3a** is an AC-HRTEM image from the edge of a CsPbBr<sub>3</sub> NS  
 227 recorded with the dose-rate of 3800 e<sup>-2</sup> s<sup>-1</sup> (exposure time 1  
 228 s). By imaging with an optimum focus and a negative spherical-  
 229 aberration,<sup>8,22</sup> we also obtain a direct structure image with Cs  
 230 and Pb–Br columns exhibiting a brighter contrast compared to  
 231 the Br columns. Looking into the details of the atomic  
 232 structure, we notice that the lower region (marked as II) of  
 233 **Figure 3a** differs structurally compared to the upper region  
 234 (marked as I). The difference is most evident in the  
 235 corresponding Fourier transforms of regions I and II as  
 236 shown in **Figure 3b,c**, respectively. The simulations of the  
 237 electron diffraction patterns of cubic and orthorhombic  
 238 CsPbBr<sub>3</sub> in a [001] zone axis orientation are provided in  
 239 **Figure 3d,e**, respectively. Comparing the experimental data with  
 240 the simulation, we can conclude that we observe the case of a  
 241 mixed structure where region I crystallized in the cubic  
 242 structure while region II is in the orthorhombic structure.  
 243 **Figure 3f,g** shows enlarged images from region I and II,  
 244 respectively, with the atomic structural model overlaid.

Experimental images agree well with the structure models, 245  
 and the tilting of the Pb–Br<sub>6</sub> octahedrons in the orthorhombic 246  
 phase is directly observable. 247

A further quantitative examination allows us to extract 248  
 additional complementary information. First, the Br displace- 249  
 ment map shown in **Figure 4a** reveals that the lower region 250  
 exhibits larger displacements from the midpoint between two 251  
 neighboring Cs columns as a result of tilting octahedrons in 252  
 orthorhombic structure. This clearly marks the boundary 253  
 between the orthorhombic and cubic phases. Second, we 254  
 have measured lattice parameters unit cell by unit cell and the 255  
 result is shown in **Figure 4b**. For bulk CsPbBr<sub>3</sub>, the distance 256  
 between Pb–Br columns in [001] projection differs by only 5 257  
 pm between cubic (5.87 Å) and orthorhombic structure (5.82 258  
 Å). Experimentally for the 2D NS, both the cubic and 259  
 orthorhombic phases exhibit a lattice expansion compared to 260  
 their bulk counterpart, but this map can still identify the 261  
 orthorhombic region from the map as it exhibits smaller 262  
 distances (blue color). The presence of a lattice expansion in 263  
 ultrathin 2D CsPbBr<sub>3</sub> NSs is confirmed by our grazing- 264  
 incidence wide-angle X-ray scattering (GIWAXS) experiments 265  
 (**Figure S13**). Finally, we have measured the tilting angle of the 266

267 Pb–Br<sub>6</sub> octahedrons and the tilting map is shown in Figure 4c.  
268 The chessboard pattern in the lower region is another clear  
269 confirmation that the orthorhombic structure is present. These  
270 results may have relevance for the understanding of the growth  
271 and structure–property relationship in the halide perovskite  
272 materials.

273 The combination of dose controlled AC-HRTEM imaging  
274 and low dose-rate in-line holography enables atomic resolution  
275 imaging of halide perovskites without introducing structural  
276 damages in CsPbBr<sub>3</sub>. The crystallographic structure of plate  
277 shaped nanocrystals is revealed at atomic resolution with single  
278 atom sensitivity. A reproducible determination of absolute  
279 phase values for electrons that are scattering at single atoms  
280 shows that the method has become fully quantitative if beam-  
281 sample interactions are controlled. We fully characterize  
282 coexisting high-temperature and low-temperature phases that  
283 are studied in this manner. Importantly, the method can be  
284 applied to any beam-sensitive material and does not require  
285 uncommon TEM attachments so that it can be easily  
286 popularized in most of the laboratories. This work shows that  
287 another door opened for atomic resolution imaging of beam-  
288 sensitive materials in general, and it can be further explored and  
289 developed, such as utilizing direct electron detection<sup>27</sup> or  
290 complementing with other low dose techniques.<sup>28,29</sup>

## 291 ■ ASSOCIATED CONTENT

### 292 ● Supporting Information

293 The Supporting Information is available free of charge on the  
294 ACS Publications website at DOI: 10.1021/acs.nano-  
295 lett.6b03331.

296 Details of materials synthesis, characterization methods,  
297 image processing and simulations, and first-principle  
298 calculations. Discussions of electron beam-sample  
299 interaction, low dose-rate imaging, and coexistence of  
300 cubic and orthorhombic phases (PDF)

## 301 ■ AUTHOR INFORMATION

### 302 Corresponding Author

303 \*E-mail: p\_yang@berkeley.edu.

### 304 Author Contributions

305 Y.Y. and P.Y. designed the experiments. Y.Y. performed TEM  
306 experiments, simulations, and data analysis. D.Z. carried out the  
307 synthesis of halide perovskite samples and performed XRD  
308 experiments. C.K. contributed to the data analysis. L.D.  
309 performed AFM experiments. N.K. performed GIWAXS  
310 experiments. Y.B. and A.B.W. contributed to the data analysis  
311 and manuscript preparation. Y.Y., C.K., and P.Y. wrote the  
312 manuscript. C.K. supervised the low dose-rate experiments.  
313 A.P.A. and P.Y. supervised the research project. All authors  
314 contributed to the discussions.

### 315 Notes

316 The authors declare no competing financial interest.

## 317 ■ ACKNOWLEDGMENTS

318 This work was supported by the Physical Chemistry of  
319 Inorganic Nanostructures Program, KC3103, Office of Basic  
320 Energy Sciences of the United States Department of Energy  
321 under Contract No. DE-AC02-05CH11231. TEM Work at the  
322 NCEM, Molecular Foundry, and GIWAXS measurements at  
323 beamline 7.3.3 at the Advanced Light Source (ALS), were  
324 supported by the Office of Science, Office of Basic Energy  
325 Science, of the U.S. Department of Energy under Contract No.

DE-AC02-05CH11231. We would like to thank Chenhui Zhu 326  
for help with GIWAXS measurements. 327

## ■ REFERENCES 328

- 329 (1) Liu, M.; Johnston, M. B.; Snaith, H. J. Efficient planar 329  
heterojunction perovskite solar cells by vapour deposition. *Nature* 330  
2013, 501, 395–398. 331
- 332 (2) Protesescu, L.; Yakunin, S.; Bodnarchuk, M. I.; Krieg, F.; Caputo, 332  
R.; Hendon, C. H.; Yang, R. X.; Walsh, A.; Kovalenko, M. V. 333  
Nanocrystals of Cesium Lead halide perovskites (CsPbX<sub>3</sub>, X = Cl, Br, 334  
and I): Novel optoelectronic materials showing bright emission with 335  
wide color gamut. *Nano Lett.* 2015, 15, 3692–3696. 336
- 337 (3) Cottingham, P.; Brutchey, R. L. On the crystal structure of 337  
colloidally prepared CsPbBr<sub>3</sub> quantum dots. *Chem. Commun.* 2016, S2, 338  
5246–5249. 339
- 340 (4) Zhang, D.; Eaton, S. W.; Yu, Y.; Dou, L.; Yang, P. Solution-phase 340  
synthesis of Cesium Lead halide perovskite nanowires. *J. Am. Chem.* 341  
*Soc.* 2015, 137, 9230–9233. 342
- 343 (5) Bekenstein, Y.; Koscher, B. A.; Eaton, S. W.; Yang, P.; Alivisatos, 343  
A. P. Highly luminescent colloidal nanoplates of perovskite Cesium 344  
Lead halide and their oriented assemblies. *J. Am. Chem. Soc.* 2015, 137, 345  
16008–16011. 346
- 347 (6) Akkerman, Q. A.; Motti, S. G.; Kandada, A. R. S.; Mosconi, E.; 347  
D’Innocenzo, V.; Bertoni, G.; Marras, S.; Kamino, B. A.; Miranda, L.; 348  
De Angelis, F.; Petrozza, A.; Prato, M.; Manna, L. Solution synthesis 349  
approach to colloidal Cesium Lead halide perovskite nanoplatelets 350  
with monolayer-level thickness control. *J. Am. Chem. Soc.* 2016, 138, 351  
1010–1016. 352
- 353 (7) Dou, L.; Wong, A. B.; Yu, Y.; Lai, M.; Kornienko, N.; Eaton, S. 353  
W.; Fu, A.; Bischak, C. G.; Ma, J.; Ding, T.; Ginsberg, N. S.; Wang, L. 354  
W.; Alivisatos, A. P.; Yang, P. Atomically thin two-dimensional 355  
organic-inorganic hybrid perovskites. *Science* 2015, 349, 1518–1521. 356
- 357 (8) Jia, C. L.; Lentzen, M.; Urban, K. Atomic-resolution imaging of 357  
oxygen in perovskite ceramics. *Science* 2003, 299, 870–873. 358
- 359 (9) Muller, D. A.; Kourkoutis, L. F.; Murfitt, M.; Song, J. H.; Hwang, 359  
H. Y.; Silcox, J.; Dellby, N.; Krivanek, O. L. Atomic-scale chemical 360  
imaging of composition and bonding by aberration-corrected 361  
microscopy. *Science* 2008, 319, 1073–1076. 362
- 363 (10) Jia, C. L.; Mi, S. B.; Urban, K.; Vrejoiu, I.; Alexe, M.; Hesse, D. 363  
Atomic-scale study of electric dipoles near charged and uncharged 364  
domain walls in ferroelectric films. *Nat. Mater.* 2008, 7, 57–61. 365
- 366 (11) Kim, Y. M.; He, J.; Biegalski, M. D.; Ambaye, H.; Lauter, V.; 366  
Christen, H. M.; Pantelides, S. T.; Pennycook, S. J.; Kalinin, S. V.; 367  
Borisevich, A. Y. Probing oxygen vacancy concentration and 368  
homogeneity in solid-oxide fuel-cell cathode materials on the 369  
subunit-cell level. *Nat. Mater.* 2012, 11, 888–894. 370
- 371 (12) Yadav, A. K.; Nelson, C. T.; Hsu, S. L.; Hong, Z.; Clarkson, J. 371  
D.; Schlepueetz, C. M.; Damodaran, A. R.; Shafer, P.; Arenholz, E.; 372  
Dedon, L. R.; Chen, D.; Vishwanath, A.; Minor, A. M.; Chen, L. Q.; 373  
Scott, J. F.; Martin, L. W.; Ramesh, R. Observation of polar vortices in 374  
oxide superlattices. *Nature* 2016, 530, 198–201. 375
- 376 (13) Nellist, P. D. The principles of STEM Imaging. In *Scanning* 376  
*Transmission Electron Microscopy*; Pennycook, S. J., Nellist, P. D., Eds.; 377  
Springer: New York, 2011; pp 91–115. 378
- 379 (14) Krivanek, O. L.; Chisholm, M. F.; Nicolosi, V.; Pennycook, T. J.; 379  
Corbin, G. J.; Dellby, N.; Murfitt, M. F.; Own, C. S.; Szilagy, Z. S.; 380  
Oxley, M. P.; Pantelides, S. T.; Pennycook, S. J. Atom-by-atom 381  
structural and chemical analysis by annular dark-field electron 382  
microscopy. *Nature* 2010, 464, 571–574. 383
- 384 (15) Kisielowski, C.; Wang, L.-W.; Specht, P.; Calderon, H. A.; 384  
Barton, B.; Jiang, B.; Kang, J. H.; Cieslinski, R. Real-time sub- 385  
Ångstrom imaging of reversible and irreversible conformations in 386  
rhodium catalysts and graphene. *Phys. Rev. B: Condens. Matter Mater.* 387  
*Phys.* 2013, 88, 024305. 388
- 389 (16) Van Dyck, D.; Jinschek, J. R.; Chen, F. R. ‘Big Bang’ 389  
tomography as a new route to atomic-resolution electron tomography. 390  
*Nature* 2012, 486, 243–246. 391

- 392 (17) Chen, F. R.; Van Dyck, D.; Kisielowski, C. In-line three-  
393 dimensional holography of nanocrystalline objects at atomic  
394 resolution. *Nat. Commun.* **2016**, *7*, 10603.
- 395 (18) Huang, C.; Borisenko, K. B.; Kirkland, A. I. Exit wave  
396 reconstruction of radiation-sensitive materials from low-dose data. *J.*  
397 *Phys.: Conf. Ser.* **2014**, *522*, 012052.
- 398 (19) Meyer, R. R.; Sloan, J.; Dunin-Borkowski, R. E.; Kirkland, A. I.;  
399 Novotny, M. C.; Bailey, S. R.; Hutchison, J. L.; Green, M. L. H.  
400 Discrete atom imaging of one-dimensional crystals formed within  
401 single-walled carbon nanotubes. *Science* **2000**, *289*, 1324–1326.
- 402 (20) Wang, A.; Chen, F. R.; Van Aert, S.; Van Dyck, D. Direct  
403 structure inversion from exit waves. *Ultramicroscopy* **2010**, *110*, 527–  
404 534.
- 405 (21) Hsieh, W. K.; Chen, F. R.; Kai, J. J.; Kirkland, A. I. Resolution  
406 extension and exit wave reconstruction in complex HREM. *Ultra-*  
407 *microscopy* **2004**, *98*, 99–114.
- 408 (22) Yu, Y.; Zhang, X.; Zhao, Y. G.; Jiang, N.; Yu, R.; Wang, J. W.;  
409 Fan, C.; Sun, X. F.; Zhu, J. Atomic-scale study of topological vortex-  
410 like domain pattern in multiferroic hexagonal manganites. *Appl. Phys.*  
411 *Lett.* **2013**, *103*, 032901.
- 412 (23) Jinschek, J. R.; Yucelen, E.; Calderon, H. A.; Freitag, B.  
413 Quantitative atomic 3-D imaging of single/double sheet graphene  
414 structure. *Carbon* **2011**, *49*, 556–562.
- 415 (24) Kashtiban, R. J.; Dyson, M. A.; Nair, R. R.; Zan, R.; Wong, S. L.;  
416 Ramasse, Q.; Geim, A. K.; Bangert, U.; Sloan, J. Atomically resolved  
417 imaging of highly ordered alternating fluorinated graphene. *Nat.*  
418 *Commun.* **2014**, *5*, 4902.
- 419 (25) Linck, M.; Lichte, H.; Lehmann, M. Off-axis electron  
420 holography: Materials analysis at atomic resolution. *Int. J. Mater. Res.*  
421 **2006**, *97*, 890–898.
- 422 (26) Zheng, H.; Sadtler, B.; Habenicht, C.; Freitag, B.; Alivisatos, A.  
423 P.; Kisielowski, C. Controlling electron beam-induced structure  
424 modifications and cation exchange in cadmium sulfide-copper sulfide  
425 heterostructured nanorods. *Ultramicroscopy* **2013**, *134*, 207–213.
- 426 (27) McMullan, G.; Clark, A. T.; Turchetta, R.; Faruqi, A. R.  
427 Enhanced imaging in low dose electron microscopy using electron  
428 counting. *Ultramicroscopy* **2009**, *109*, 1411–1416.
- 429 (28) Buban, J. P.; Ramasse, Q.; Gipson, B.; Browning, N. D.;  
430 Stahlberg, H. High-resolution low-dose scanning transmission electron  
431 microscopy. *J. Electron Microsc.* **2010**, *59*, 103–112.
- 432 (29) Meyer, J. C.; Kotakoski, J.; Mangler, C. Atomic structure from  
433 large-area, low-dose exposures of materials: a new route to circumvent  
434 radiation damage. *Ultramicroscopy* **2014**, *145*, 13–21.